AN IMAGING, TUNABLE MAGNETO-OPTICAL FILTER

H. LIN and J. R. KUHN

Department of Physics and Astronomy, Michigan State University, East Lansing, MI 48824, U.S.A.

(Received 11 December, 1988)

Abstract. The Imaging, Tunable Magneto-Optical Filter (ITMOF) is a one- or two-cell magnetic birefringence filter designed to measure the Doppler shift of the solar potassium line (770 nm) with respect to a laboratory standard. Two gas vapor cells contain isotopically refined potassium and operate at temperature near 393 K. Hot cell windows are employed in a carefully controlled thermal environment to limit spurious birefringence in the pyrex cell and prevent condensation in the light path. Electromagnets provide a variable strength and direction longitudinal magnetic field of up to 5000 G on each cell. There is no rotating quarter-wave plate or other moving parts. The final image is detected with a CCD camera system.

1. Introduction

The use of an atomic resonance cell provides an accurate and stable frequency reference for Doppler velocity shift measurements. One was used in a scattering mode by Brookes, Isaak, and van der Raay (1978). In their spectrometer, the narrow-band circularly polarized sunlight is scattered near the two Zeeman frequencies from a sodium vapor cell embedded in a permanent magnet. The sense of circular polarization determines whether the blue or the red component of the spectrum is to be scattered. The difference between the intensity of the two components, divided by the sum, is a measure of the Doppler shift of the absorption line. The velocity noise of this spectrometer was approximately 1 m s^{-1}. However, their spectrometer sums all the light from the solar image, which has an important drawback. The spatial information of the oscillation is lost in the averaging process. Also, the transparency variations in the Earth's atmosphere can alter the position and the shape of the solar line profile, which introduces additional noise in the velocity measurement.

The resonant cell can also be used as a magneto-optical filter (MOF). In this mode, the intensity of the transmitted light, instead of the scattered light, is measured. The advantage is that it preserves the spatial information and enables one to obtain three dimensional (X, Y, T) information. With a spatially-resolved velocity map of the entire solar disk, one can identify the oscillation modes with intermediate l values. These modes yield mode informations about the solar interior. However, the amplitudes are low, typically less than 20 cm s^{-1}.

The working principle of the MOF was first introduced by Cacciani, Cimino, and Sopranzi (1968). It was later used by Agnelli, Cacciani, and Fofi (1975) and Cacciani and Fofi (1978) for solar observation. Rhodes *et al.* (1985) developed a two-cell MOF based on the design of Cacciani. This MOF transmits the light at one of the two Zeeman frequencies. Their MOF employed two sodium vapor cells with permanent magnets. It also required a rotating quarter-wave plate to select the transmission component. They

Solar Physics **122:** 365–380, 1989.

obtained the first three-dimensional data set useful for solar oscillation observations. This instrument was later used for the study of the rotational frequency splitting of the five-minute oscillations (Tomczyk, 1988). With permanent magnets, the bandpass frequency of a MOF is tunable only by changing the optical depth of the vapor, and the change in optical depth also changes the bandwidth. At high optical depth, the transmission profile of the MOF becomes complicated, which makes selection of the transmission components difficult. In this paper we report on an Imaging, Tunable Magneto-Optical Filter (ITMOF). The ITMOF employs potassium vapor cells and electromagnets instead of permanent magnets used by the MOF. The electromagnets provide different operating modes for the ITMOF, and the vapor cells are operated at low temperature and optical depth. Moreover, this design eliminates the need of a rotating quarter-wave plate. Hence, the instrument does not have any moving components. The ITMOF, when used with a CCD camera, can obtain spatially-resolved velocity maps of the whole solar disk.

2. Principles

The dielectric constant of circularly polarized light as a function of frequency can be written as

$$\varepsilon_{\pm} = 1 + \frac{\omega_p^2}{-\omega^2 + \omega_0^2 \pm \omega_B \omega - i\gamma\omega}, \tag{2.1}$$

where + and − subscripts represent the left and right circular polarizations, ω_0 is the $B = 0$ resonance frequency of the potassium vapor (769.9 nm), ω_B is the synchrotron frequency, ω_p is the plasma frequency, and γ is the atomic damping constant. If we express the wave-number k of a plane wave as $k = \beta + i\alpha/2$ with $\alpha = (\sqrt{2}\,\omega/c)\,(-\mathrm{Re}(\varepsilon) + \sqrt{\mathrm{Re}^2(\varepsilon) + \mathrm{Im}^2(\varepsilon)})^{-1/2}$ and $\beta = \mathrm{Im}(\varepsilon)\alpha$, then the state vector of the light emerging from the vapor cell can be written as

$$\mathbf{E} = \frac{E_0}{2}\,(e^{ik_+ z - i\omega t}\hat{\mathbf{e}}_+ + e^{ik_- z - i\omega t}\hat{\mathbf{e}}_-), \tag{2.2}$$

where k_+ and k_- are the wave number of the positive and negative circularly polarized light, respectively. Note that from Equation (2.1), it is obvious that $\varepsilon_+ = \varepsilon_-$ when $\omega_B = 0$, i.e., when $B = 0$. The effect of the vapor in a magnetic field on circularly polarized light is to partially absorb and retard the light near the two Zeeman frequencies. For linearly polarized incident light, the effect is then to rotate the polarization plane of the incident light. When a second linear polarizer is placed behind the cell with its plane of polarization perpendicular to that of the incident light, the total intensity transmitted through it is

$$I = \frac{\varepsilon}{8\pi}\,|\mathbf{E}|^2 =$$

$$= \frac{\varepsilon}{8\pi}\,\frac{|E_0|^2}{4}\,(e^{-\alpha_+ z} + e^{-\alpha_- z} - 2e^{(\alpha_+ + \alpha_-)z/2}\cos((\beta_+ - \beta_-)z)). \tag{2.3}$$

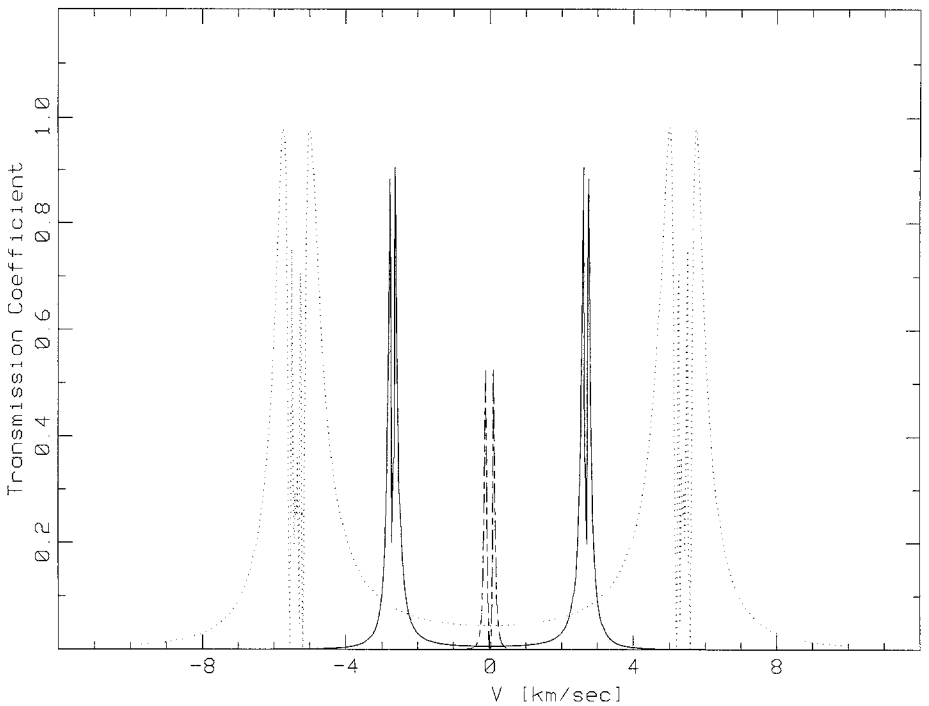

Fig. 1. The calculated transmission profiles of the linear polarizers and cell assembly (the narrow bandpass filter). The dashed line is calculated with B = 10 G and T = 373 K. The solid line is calculated with B = 2500 G and T = 373 K. The dotted line is calculated with B = 5000 G and T = 393 K.

The calculated transmission coefficient of Equation (2.3) as a function of frequency with different magnetic fields and cell temperatures is plotted in Figure 1. The vapor density is calculated according to the formula (Zeng *et al.*, 1985)

$$n = \frac{1}{T}\, 10^{(27.43 - 3964/T)}. \tag{2.4}$$

The linear polarizer and cell combination thus acts as a narrow band-pass filter with a tunable center frequency and width. At low optical depth, the position of the transmission peaks are determined by the magnetic field, while the bandwidth is controlled by the cell temperature. When $B = 0$, $\varepsilon_+ = \varepsilon_-$, hence, $\alpha_+ = \alpha_-$ and $\beta_+ = \beta_-$, and, hence, $I = 0$. Thus the filter can be 'turned off' by turning off the magnetic field. Although in practice, the residual magnetic field is never strictly zero, and an appreciable transmission peak remains at low-magnetic field.

In the case of circularly polarized incident light, $\mathbf{E}_{\text{in}} = E_0\, e^{ik_\pm z - i\omega t}\hat{\mathbf{e}}_\pm$, the transmitted intensity as a function of frequency can be expressed as

$$I = \frac{\varepsilon}{8\pi}\,\frac{|E_0|^2}{4}\, e^{\alpha_\pm z}. \tag{2.5}$$

This intensity, multiplied by the intensity of Equation (2.3), gives the transmission profile of the two-cell configuration. Figure 2 shows the transmission profile for the circularly polarized incident light. As in the case of linearly polarized incident light, the width and

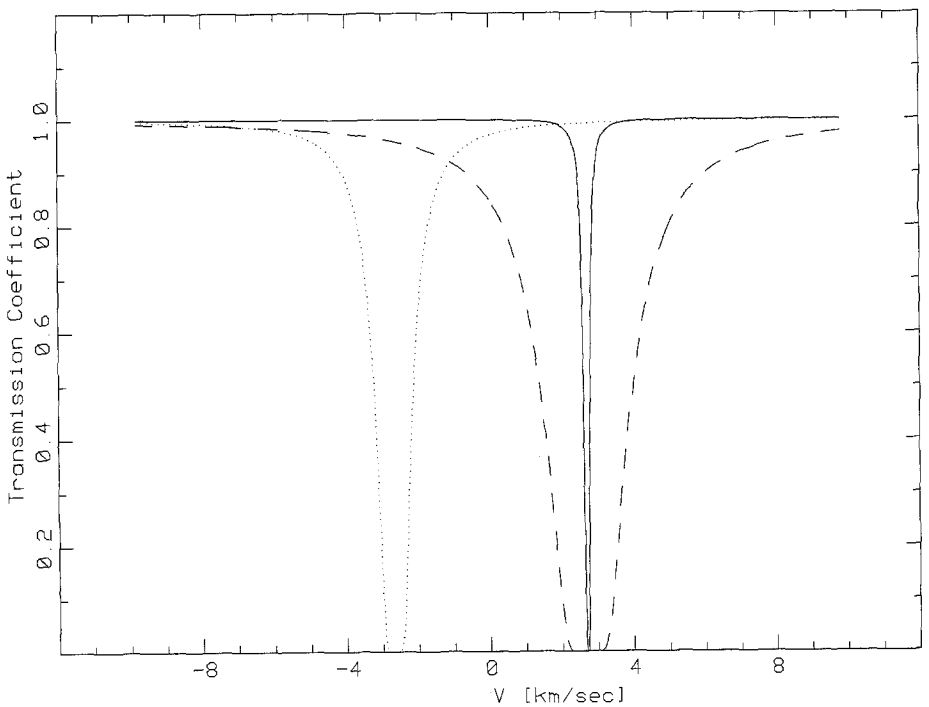

Fig. 2. The calculated transmission profiles of the quarter-wave plate and cell assembly (the wing selector). The solid line is calculated with $B = 2500$ G and $T = 373$ K. The dotted line is calculated with $B = -2500$ G and $T = 423$ K. The dashed line is calculated with $B = 2500$ G and $T = 453$ K.

position of the absorption region are controlled by temperature and magnetic field, respectively. The absorption region appears only at one side of the spectrum for one direction of magnetic field. If the direction of the magnetic field of the second cell is reversed, the absorption region will appear on the other side of the spectrum. Thus, we can select either the red or the blue component to be transmitted by selecting the direction of magnetic field.

3. The Instrument

3.1. The ITMOF

The ITMOF observes the oscillation velocity of the Sun by measuring the Doppler shift of the solar potassium line. Figure 3 is the system block diagram of the two-cell configuration of the instrument. The first stage is a combination of a 'cold' mirror, which

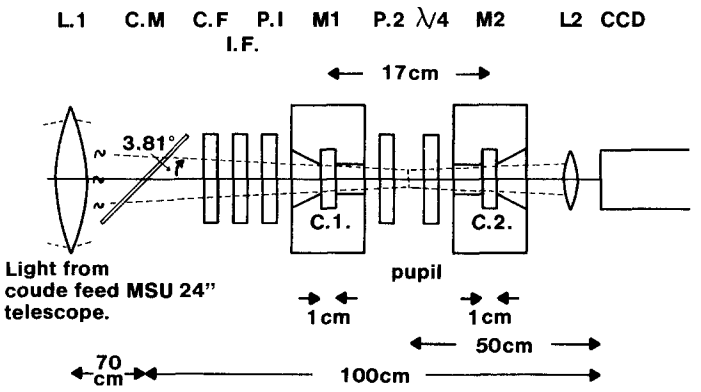

System Block Diagram

Fig. 3. System block diagram of the ITMOF. L.1: Lens 1, f = 100 cm; C.M: Cold Mirror; C.F: Coarse Filter; I.F.: Interference Filter; P.1: Linear Polarizer 1; M1: Electromagnet 1; C.1.: Potassium Vapor Cell 1; P.2: Linear Polarizer 2; $\lambda/4$: quarter wave plate; M2: Electromagnet 2; C.2.: Potassium Vapor Cell 2; L2: lens 2, f = 30 cm; CCD: TI-4889 CCD camera.

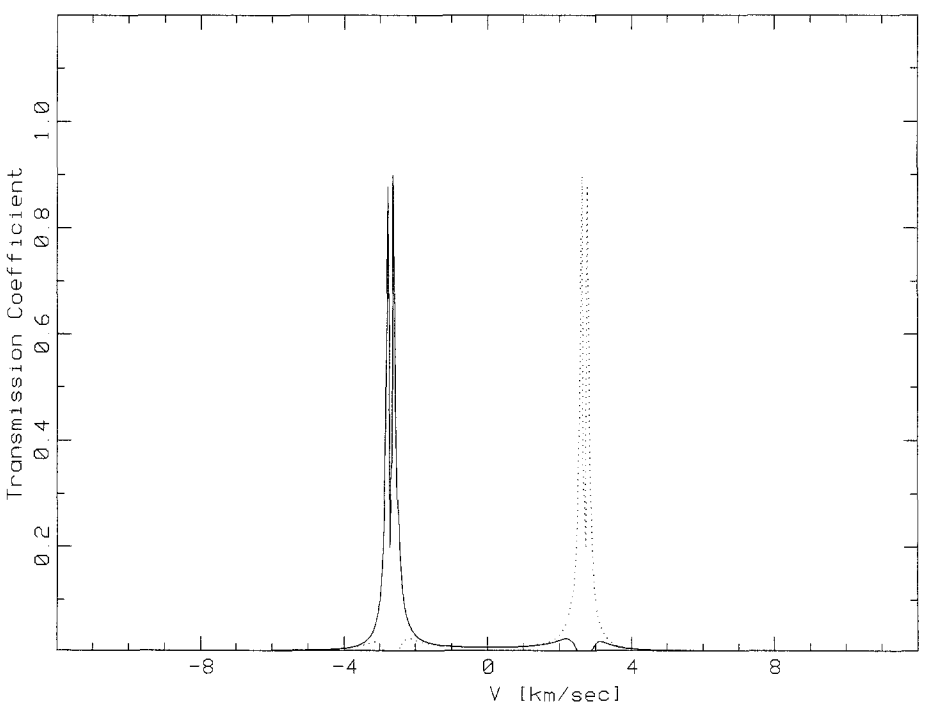

Fig. 4. The transmission profiles of the two-cell configuration. The solid line is calculated with B_{cell_1} = 2500 G and B_{cell_2} = 2500 G. The dotted line is calculated with B_{cell_1} = 2500 G and B_{cell_2} = −2500 G. The temperatures of the first and second cell are 353 K and 423 K, respectively.

removes heat and short wavelength radiation, a coarse filter, and a narrow bandwidth interference filter. The resulting bandwidth of this filter combination is approximately 1 nm centered at 769.9 nm.

The second stage consisted of two linear polarizers with their planes of polarization perpendicular to each other, and a magnet-cell assembly placed between the two polarizers. This stage acts as a tunable narrow band-width filter.

The third stage is the wing-selector, which consisted of a circular polarizer and a second magnet-cell assembly. One of the two transmitted components from the first cell, after been circularly polarized, is partially absorbed by the vapor. The direction of the magnetic field determines which component is to be absorbed. Hence, we can select to pass only the red or blue component by reversing the direction of the magnetic field without rotating the quarter wave plate. Figure 4 shows the calculated transmission profiles of the third stage combined with the second stage for the two directions of the field.

3.2. Operation Modes

The ITMOF can be operated in either a one-cell or two-cell configuration. Below we will compare the performance characteristics of the system in these two modes.

3.2.1. *One-Cell Mode*

The one-cell configuration uses the first stage (the filters assembly), and the second stage (the narrow band-width filter). Three images with $B = 0$, $B = B_1$, and $B = B_2$ were taken. The ratio of the intensity modulation of B_2 and B_1 is a measure of the Doppler shift:

$$r_1 = \frac{I_{B_2} - I_{B_1}}{I_{B_1} - I_0} \,. \tag{3.1}$$

The velocity sensitivity of I_{B_1} and I_{B_2} varies with the magnetic field strength. At small operating field when the wavelength difference between the red and blue transmission peaks is much smaller than the width of the potassium line, the transmission profile can be regarded as a single transmission peak at the potassium absorption frequency, and the corresponding I_B measures the intensity at different position of the absorption line due to the velocity shift of the spectrum. When the operating magnetic field is large, such that the wavelength difference between the red and blue transmission peaks is approximately equal to the width of the potassium line, the velocity sensitivity arise from the asymmetry of the line profile. In either case, the velocity sensitivity is small when the transmission peaks are centered on the line profile. However, with suitably chosen B_1 and B_2, we can maximize the velocity sensitivity of r_1. Figure 5 shows the calculated velocity response of different combinations of magnetic field. The calculations were done with the solar potassium line profile taken from the center of the solar disk using data obtained from Sacramento Peak Observatory. The FWHM of this profile is $\sim 6\ \mathrm{km\ s^{-1}}$.

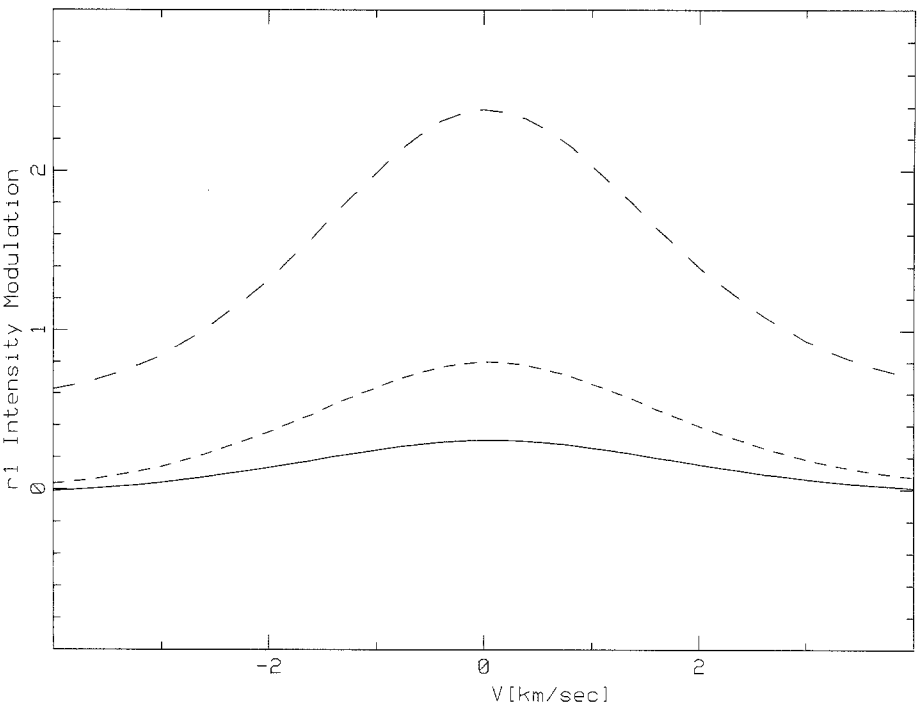

Fig. 5. The calculated velocity response of the one-cell configuration. The cell temperature is 373 K. The long dash line is calculated with B_1 = 625 G and B_2 = 2500 G. The short dash line is calculated with B_1 = 1250 G and B_2 = 2500 G. The solid line is calculated with B_1 = 1875 G and B_2 = 2500 G.

The intensity I_0 is different from I_{dark}, the dark current of the CCD detector, due to the finite extinction ratio of the crossed polarizers. There are also contributions from the birefringent effect of the cell windows. Moreover, a residual magnetic field exists, even when the magnet is turned off. The magnitude of this residual field is of the order of a few gauss, and the peak transmission coefficient for this field is about 0.5, as in Figure 1. This is large enough to generate a velocity-sensitive signal in I_0. However, this signal is small compared with that from the large magnetic field B_1 and B_2, hence, $I_{B_1} - I_0$ is still a good approximation for the intensity modulation due to B_1.

3.2.2. *Two-Cell Mode*

The one-cell configuration makes use of the asymmetry of the red and blue transmission peaks with respect to the solar potassium line profile. Since this asymmetry is small, the velocity sensitivity in these modes are comparatively smaller. To improve the velocity sensitivity, the ITMOF can be operated in a two-cell mode. The two-cell configuration takes two images at the red and blue wing of the spectrum. Another image is then taken with $B_1 = 0$. The dimensionless quantity r_2 is then calculated according to

$$r_2 = \frac{I_r - I_b}{I_r + I_b} . \tag{3.2}$$

The velocity sensitivity of r_2 is about an order of magnitude larger than that of the one-cell configuration. It can also be tuned to have nearly linear r_2 response by tuning the operating magnetic fields. However, the velocity response depends not only on the magnetic field, but also on the shift of the spectrum. The velocity field due to the solar rotation across the solar disk is large enough that there is a nonlinear response over the whole solar disk.

3.3. Vapor cell and temperature control

The vapor cells are made of pyrex glass, with diameter equal to 2.1 cm and length equal to 1 cm (Figure 6). The cell was evacuated to 10^{-5} torr and then K^{39} was injected into

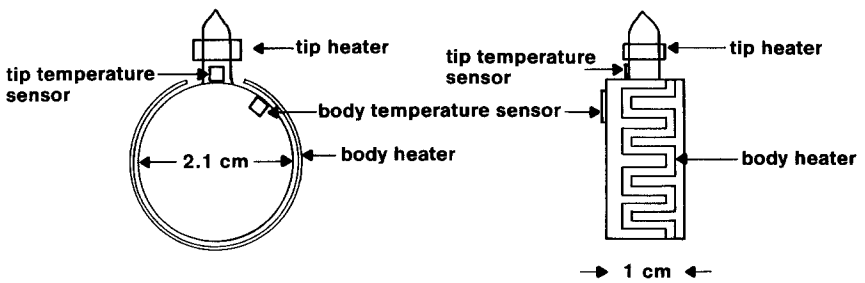

Fig. 6. The potassium vapor cell, heaters, and temperature sensors.

it before being sealed. The absorption spectrum of potassium is complicated by the presence of the two stable isotopes, K^{39} and K^{41}. The natural abundance ratio of K^{39} to K^{41} is 13.5:1. The isotope shift is 176 m s^{-1} (Jackson and Kuhn, 1938). The position of the centroid is shifted by 76 m s^{-1}. when the optical depth changes from optically thin to thick. We use 99.7% refined K^{39} isotope, which reduces the isotope shift to less than 1 m s^{-1}. To further reduce the noise induced by the variation of optical depth, the temperature of the cells are carefully controlled to a variation of less than $\pm$ 1 K. In order to achieve this stability, the cells are placed in a vacuum chamber on a cell housing to prevent convection between the cells and the surrounding atmosphere, while the temperature of the cell housing is kept at constant (298 K) by a recirculating liquid cooler. This makes the optical depth insensitive to ambient temperature variation.

The cell temperature is controlled by two heaters, designated a body heater, and a tip heater. The body heater wraps around the body of the cell, and the tip heater wraps around a small extension of the cell body, which is a glass tube where the cell was sealed. In addition, there are two temperature sensors, one attached to the cell body, and the other attached to the tip. The sensors are Pt resistance thermometers. The temperature signals are used for servo controlling the heaters, and also can be read out and recorded by the computer. The temperature of the body and the tip can then be controlled to vary

less than 1 K. In order to prevent potassium deposition on the cell windows, the temperature at the body is set to be approximately 10 K higher than that of the tip, thus potassium condensation occurs at the tip. However, this temperature gradient across the cell introduces a non-uniform distribution of vapor, and thus produces a non-uniform transmission property across the solar image. But this is not a serious problem because the fractional intensity modulation from each points on the solar image, instead of the absolute intensity, is used to calculate the Doppler shift.

3.4. Electromagnet and Magnetic Field Control

The cell housing is embedded in an electromagnet (Figure 7) which is capable of producing a magnetic field up to 5000 G in the direction parallel to the optical path. A Hall probe, attached to the cell housing near the window, returns the magnetic field to a servo-control circuit, as well as to the computer for monitoring and recording pur-

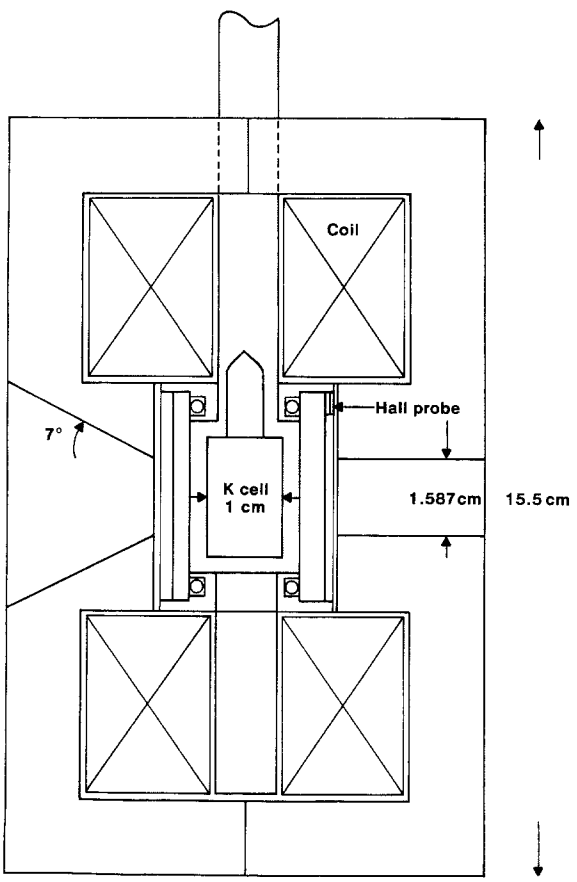

Fig. 7. The vapor cell and magnet assembly. The vacuum region is pumped from the tube that enters the cell housing from above.

poses. The magnet consisted of two coils with two soft-iron pole pieces. The power dissipation is approximately 170 W to generate 5000 G field.

3.5. Optical system

We used the 0.6 m modified Cassegrain telescope located at MSU observatory to test the performance characteristics of the ITMOF. To reduce the amount of light collected by the telescope, a mask with a 1.5 cm diameter aperture is placed at the entrance pupil of the telescope. The light from the coudé feed of the telescope is directed into the ITMOF. A 100 cm and a 30 cm focal length lenses are used to form the solar image near the first potassium vapor cell. However, since the telescope was not designed for solar observation, it produced a drift of the solar image, which limited the useful duration of a single observation sequence to less than 1 hour.

3.6. Computer control and data acquisition

The ITMOF is controlled by an IBM PC-AT computer, equipped with a 9-track tape drive for data acquisition. A TI-4889 384 × 584 pixels CCD camera is employed to register the picture of the Sun. The interface between the computer and the electromagnets use a two channel, 12 bits D/A converter, which controls the power supplies for the electromagnets. Another 6 channels 12 bits A/D converter returns the temperature and magnetic field at each cell.

The intensity at each pixel of the solar image was stored as a 12 bit binary number. In our present optical system, the Sun forms a 100 × 100 pixels picture. Typical exposure time is 500 ms for each picture. Added with the time required for picture storage and magnetic field setting, we can obtain an image every 8 s. Since the images taken during observation were analyzed by another VAX750 computer, the images were stored in magnetic tape directly without any manipulation. With this frame taking rate, we accumulated 16 mega-byte of data in one hour. In the case of two-cell mode operation, 4 images are used to obtain an intensity modulation map. Hence, we can obtain a velocity map each 32 s. In one-cell mode operation, the time resolution will be higher.

4. Primary Result

We have obtained velocity maps using the one-cell configuration. The magnetic and temperature modulations were also measured to compare with model calculations.

4.1. Temperature and magnetic field modulation

The fractional intensity modulation due to an applied magnetic field B was calculated according to

$$r = \frac{I_B - I_0}{I_0 - I_{\text{dark}}} \,. \tag{4.1}$$

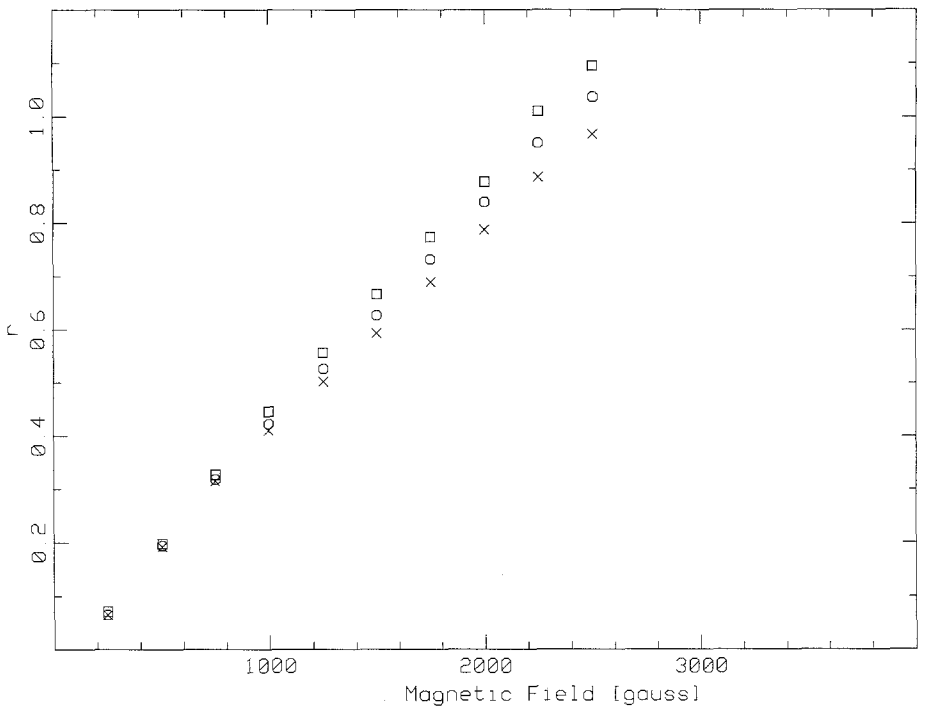

Fig. 8. The magnetic field response of the intensity modulation after averaging over different size area in the solar image plane. Square – 5 × 5 pixel area. Circle – 50 × 50 pixel area. Cross – 90 × 90 pixel area. The 90 × 90 pixel curve is approximately full-disk coverage.

At low optical depth, the $r - B$ curves measure the shape of the solar absorption line profile. The observed $r - B$ curves are plotted in Figure 8. Each curve is computed by averaging the data in a square region near the center of the solar disk. The decrease of the slope of these curves with the increase of the size of integration area in Figure 8 shows the rotational broadening effect of the line profiles.

By comparing the slope of the measured $r - B$ curves with that from model calculation at large enough field strength, we can estimate the width of the measured line profile. Calculation shows that the 10 × 10 pixels (200″ × 200″) curve has the same slope as the profile used for the model calculation. Extrapolation of the 90 × 90 pixels (1800″ × 1800″) curve shows that the width of this profile is approximately 8 km s^{-1}, in agreement with the width of ~ 8.5 km s^{-1} for profile integrated over the full solar disk.

The change of optical depth changes the wavelength transmission profile, which in turn, changes the measured intensity. When the magnetic field is high enough, the two transmission peaks are well separated, and the measured intensity increase is proportional to the increase in temperature. At low magnetic field, the two transmission peaks overlap, and the measured line profiles will be distorted. Figure 9(a) shows the measured $r - B$ curves from a 10 × 10 pixels region near the center of the solar disk at 383 K and 393 K operating temperature, normalized at 2500 G. Figure 9(b) shows the

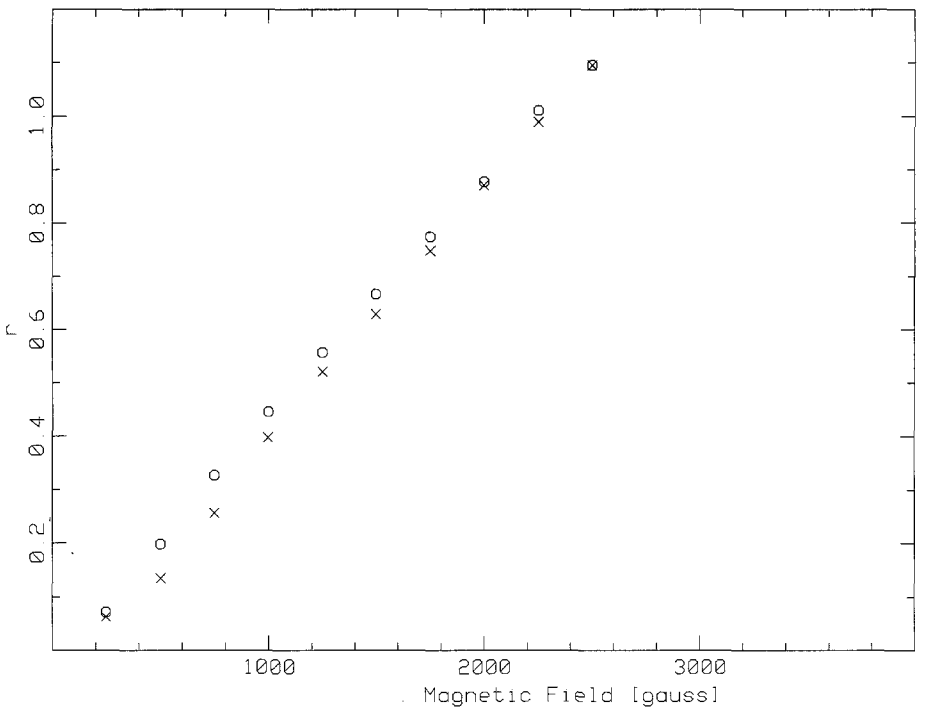

Fig. 9a. The measured $r - B$ curves normalized at $B = 2500$ G. Circle – $T = 383$ K. Cross – $T = 393$.

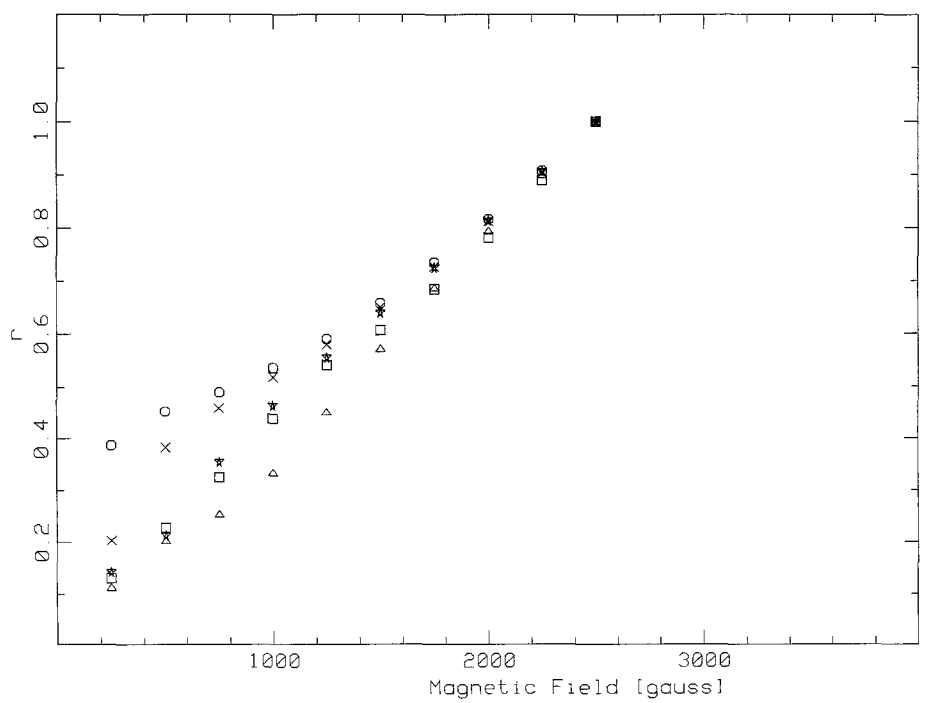

Fig. 9b. The calculated $r - B$ curves for five temperatures, normalized at $B = 2500$ G. Circle – $T = 353$ K. Cross – $T = 363$ K. Star – $T = 373$ K. Triangle – $T = 383$ K. Square – $T = 393$ K.

same curves from model calculations, with temperature ranging from 353 K to 393 K. The features in the measured $r - B$ curves show nice agreement with model calculations.

4.2. Velocity Calibration

There are several ways of calibrating the data to obtain Doppler velocity. For example, we can observe the intensity modulation near the center of the solar disk over a period of time. The change in the line-of-sight velocity due to the Earth's rotation during this period can be used to calibrate the intensity change. Another method is to use the Sun's rotational velocity field along the solar equator. Figure 10 is the r_1 modulation map of

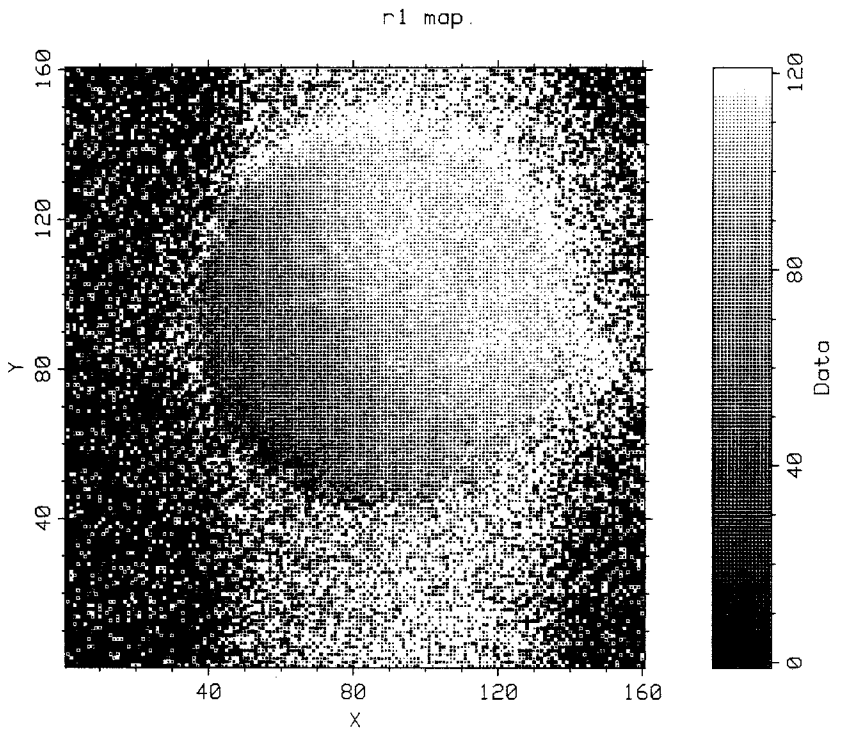

Fig. 10. The r_1 map obtained using the one-cell configuration. The operating temperature was 383 K, with B_1 = 1250 G and B_2 = 2500 G. The unit of the scale is %.

the entire solar disk taken with B_1 = 1250 G and B_2 = 2500 G. The solar rotation is clearly visible. Figure 11 shows the r_1 variation averaged over a 5 pixel-wide strip along the solar equator of Figure 10. The observed line-of-sight velocity on the solar disk is the sum of several components, $V_{obs} = V_{rot} + V_{grs} + V_{orb} + V$, where V_{rot} is the velocity due to Earth's rotation, V_{grs} is the gravitational redshift, V_{orb} is the orbital velocity of the Earth around the Sun, and V is the rotational velocity field of the Sun along the solar equator, plus the radial velocity of the solar oscillation. V_{orb}, V_{rot}, and V_{grs}, which has magnitude 640 m s^{-1} (Allen, 1963), can all be considered constant for each velocity

map. The combined magnitude of the first three terms, which is the line-of-sight velocity at the center of the solar disk at the observation time, is 1100 m s^{-1} for the image of Figure 10.

The largest term that contributes to the velocity gradient is the term V arises from solar rotation. V can be approximated by $V = V_0 d/R$, where d is the projected distance along the solar equator, R is the radius of the solar disk, and V_0 is the equatorial rotation velocity of the Sun. The magnitude of V_0 is 2000 m s^{-1} (Allen, 1963). According to model calculations, the maximum of r_1, which corresponds to zero line-of-sight velocity, should be at a distance approximately 25 pixels away from the center, which shows nice agreement with observation. The line-of-sight velocity at distance -50 pixels and $+50$ pixels in Figure 11 is 3100 m s^{-1}, and -900 m s^{-1}, respectively. Because of the

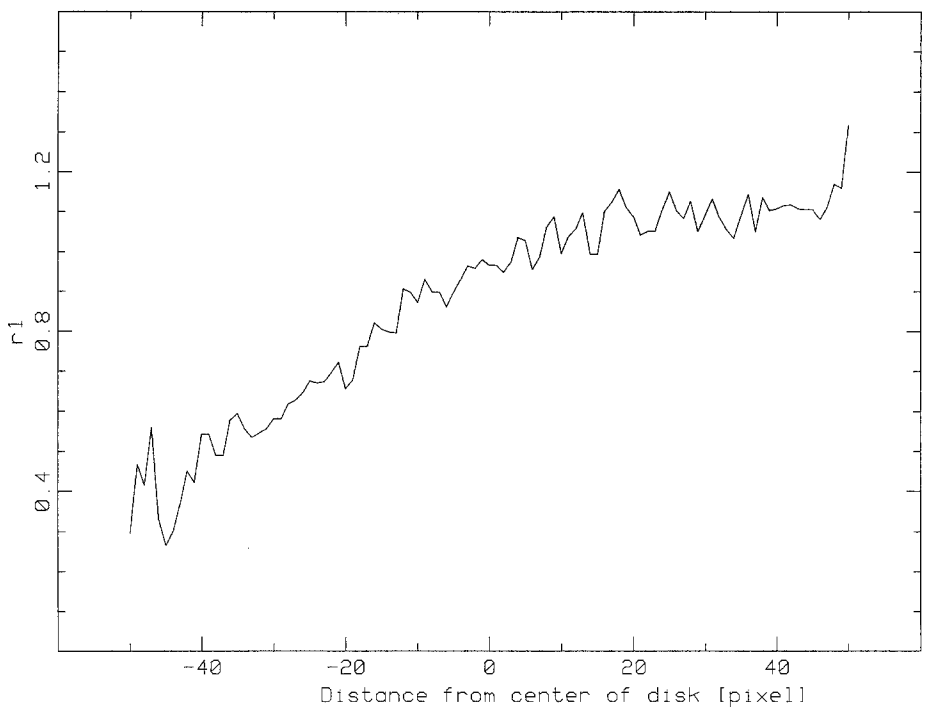

Fig. 11. The r_1 variation along the solar equator of Figure 10. The curve was obtained by averaging over a 5 pixel-wide strip along the solar equator.

nonlinear response of the operating mode, nonlinear velocity calibration must be used when converting the Doppler signal to velocity. For the linear part of the $r_1 - B$ curve in Figure 11, from -50 pixel to 10 pixel, the intensity modulation can be calibrated by the relation $V_{obs} = kr_1 + C$. It is found that $k = 2.8$ km s^{-1}, and $C = 4$ km s^{-1} for Figure 11.

5. Instrumental Errors

Since the intensity modulation was calculated on a pixel-to-pixel basis, the non-uniform transmission of the optical components will not produce any significant error in the observed intensity modulation. Clearly, sky transparency variations also will not produce any significant error. However, care must be taken when using the ITMOF in integrated-flux mode, as the non-uniform transmission property will alter the line-profile of the absorption line.

During observation, the magnetic field was turned on and off sequentially. Errors in the field strength shift the position of the bandpass windows, and produce errors in the velocity measurement. The magnetic field noise sensitivity can be calculated using the model described above. In one-cell mode operation with $B_2 = 2500$ G, $B_1 = 1250$ G, and $T = 373$ K, a 1 G shift in magnetic field produces an error of 8 m s^{-1}. The repeatability of the electromagnet was found to be better than 1 G. This limits the magnetic field noise to less than 8 m s^{-1}.

The fluctuation of the temperature of the vapor cell changes the optical depth. The theoretical velocity noise due to a 1 K change of temperature is 150 m s^{-1} for $B_1 = 1250$ G, $B_2 = 2500$ G, and $T = 373$ K. The observed temperature fluctuation was less than 0.5 K, corresponds to a 75 m s^{-1} noise contribution. Occasional large, apparently non-thermal temperature fluctuation were observed. We believe the actual temperature stability was better than our temperature noise measurements because of additional noise in the temperature reading electronics. Hence, the true temperature noise is probably less than 75 m s^{-1}. However, this is still the largest source of noise of the instrument in the one-cell configuration. In two-cell configuration, model calculations indicate a temperature fluctuation of 1 K corresponding to a velocity noise of about 1 m s^{-1}.

The observed single-pixel noise of the one-cell mode in the instrument now is approximately 300 m s^{-1}. For a 50 × 50 pixel region of the Sun, with 20 s/picture frame rate, the statistical noise level is 45 cm s^{-1} hr^{-1}. Observing over 10 hours, the statistical velocity sensitivity will be 14 cm s^{-1} 10 hr^{-1}.

6. Summary

The operating principle, as well as the possible operating modes of ITMOF, are discussed. The performance characteristics of one-cell configuration were tested. The results show nice agreement with model calculations. The next step will be to test the performance characteristics of the two-cell configuration, and to use it for the observation of solar oscillations with a new heliostat light feed.

Acknowledgements

We would like to thank Sacramento Peak Observatory for providing the solar spectrum. This research was supported by the Research Corporation, grant No. 10486.

References

Agnelli, G., Cacciani, A., and Fofi, M.: 1975, *Solar Phys.* **44**, 509.
Allen, C. W.: 1963, *Astrophysical Quantities*, 2nd ed., Athlone Press, London.
Brookes, J. R., Isaak, G. R., and van der Raay, H. B.: 1978, *Monthly Notices Roy. Astron. Soc.* **185**, 1.
Cacciani, A. and Fofi, M.: 1978, *Solar Phys.* **59**, 179.
Cacciani, A., Cimino, M., and Sopranzi, N.: 1968, *Solar Phys.* **3**, 628.
Jackson, D. A. and Kuhn, H.: 1938, *Proc. Roy. Soc. London* **A165**, 303.
Rhodes, E. J., Jr., Howard, R. F., Ulrich, R. K., and Smith, E. J.: 1983, *Solar Phys.* **82**, 245.
Rhodes, E. J., Jr., Cacciani, A., Blamont, J., Tomczyk, S., Ulrich, R. K., and Howard, R. F.: 1985, in R. K. Ulrich (ed.), *Solar Seismology from Space*, JPL Publication 84-84, 125.
Tomczyk, S.: 1988, Ph.D. Dissertation, UCLA.